The Astrophysical Journal Letters, 1011:L8 (12pp), 2026 November 1 https://doi.org/10.3847/2041-8213/aeb00b
© 2026. The Author(s). Published by the American Astronomical Society.
OPEN ACCESS

Improved Constraints on the Surface of LHS 3844 b from Its Mid-infrared Spectrum

Kimberly Paragas[1], Heather A. Knutson[1], Renyu Hu[2,3,4,5,6], Bethany L. Ehlmann[1,7,8,9], Aishwarya R. Iyer[10,13], Sebastian Zieba[11], and Laura Kreidberg[12]
[1] Division of Geological and Planetary Sciences, California Institute of Technology, USA; kparagas@caltech.edu
[2] Department of Physics and Astronomy, Rutgers, The State University of New Jersey, Piscataway, NJ 08854, USA
[3] Department of Astronomy & Astrophysics, The Pennsylvania State University, University Park, PA 16802, USA
[4] Center for Exoplanets and Habitable Worlds, The Pennsylvania State University, University Park, PA 16802, USA
[5] Institute for Computational and Data Science, The Pennsylvania State University, University Park, PA 16802, USA
[6] Jet Propulsion Laboratory, California Institute of Technology, Pasadena, CA 91109, USA
[7] Laboratory for Atmospheric & Space Physics, University of Colorado Boulder, CO 80309, USA
[8] Department of Earth Science, University of Colorado Boulder, CO 80309, USA
[9] Department of Astrophysical & Planetary Sciences, University of Colorado Boulder, CO 80309, USA
[10] NASA Goddard Space Flight Center, Greenbelt, MD 20771, USA
[11] Center for Astrophysics, Harvard & Smithsonian, Cambridge, MA 02138, USA
[12] Max-Planck-Institut für Astronomie, D-69117 Heidelberg, Germany
Received 2026 September 14; revised 2026 September 29; accepted 2026 October 1; published 2026 October 23

Abstract

The thermal emission spectra of terrestrial exoplanets provide a window into their surface compositions and corresponding geological processes. Close-in rocky planets orbiting M dwarfs are ideal targets for these studies, as observations have shown that most have little to no atmosphere. LHS 3844 b is an ultrashort-period super-Earth orbiting a nearby M dwarf, and is the most favorable target that does not have a dayside magma ocean. We present an updated JWST/MIRI Low Resolution Spectroscopy emission spectrum (5–12 μm) of this planet, derived from eight new and three archival eclipse observations. We combine these visits to obtain the highest signal-to-noise ratio (SNR) emission spectrum for any rocky exoplanet thus far, with a median SNR of 29 across 12 wavelength bins. Our data are sensitive to the predicted Si–O stretching feature (the strongest mid-infrared silicate feature) for a wide range of common materials, and the transparency feature, which is relatively insensitive to composition and constrains the grain size and porosity of surface materials. We find that LHS 3844 b's emission spectrum resembles a blackbody shortward of 10 μm, disfavoring the presence of a transparency feature, and identify a tentative feature ($1.9\sigma-3.5\sigma$) between 10 and 12 μm. If this feature is astrophysical and not instrumental in nature, it can be matched by a fayalite (the iron end-member of olivine) surface, but might also be consistent with other candidate planet-forming materials like spinel or silicon carbide. We discuss possible biases introduced by the wavelength-dependent instrumental ramp, and outline several strategies to mitigate this effect in future observations of LHS 3844 b.

Unified Astronomy Thesaurus concepts: Exoplanet surfaces (2118); Exoplanets (498); James Webb Space Telescope (2291)

Materials only available in the online version of record: data behind figures

1. Introduction

Enabled by the unprecedented sensitivity of JWST, the search for atmospheres on rocky exoplanets orbiting M dwarfs has become one of the leading pursuits in exoplanetary science (L. Kreidberg & K. B. Stevenson 2025). Over the past 5 yr, a wide range of JWST programs has searched for evidence of atmospheric features in the transmission and emission spectra of these planets, including the ongoing 500 hr Rocky Worlds Director's Discretionary Time (DDT) program. These surveys indicate that most of these rocky planets have little to no atmosphere (L. Kreidberg et al. 2019; I. J. M. Crossfield et al. 2022; T. P. Greene et al. 2023; S. Zieba et al. 2023; M. Weiner Mansfield et al. 2024; Q. Xue et al. 2024, 2025; M. Zhang et al. 2024; N. H. Allen et al. 2025; M. Fortune et al. 2025; R. Luque et al. 2025; E. A. Meier Valdés et al. 2025; P. Wachiraphan et al. 2025; N. J. Connors et al. 2026; M. Gillon et al. 2026; M. Holmberg et al. 2026; A. Rochon et al. 2026), aside from the subset that are able to maintain atmospheres via sustained outgassing from a molten dayside or tidally driven volcanism (e.g., R. Hu et al. 2024; A. Bello-Arufe et al. 2025; C. Monaghan et al. 2025; J. K. Teske et al. 2025; B. P. Coy et al. 2026).

The airless rocky planets present a valuable opportunity for surface characterization via thermal emission measurements in the near-infrared (NIR) and mid-infrared (MIR). Different surfaces will exhibit distinct spectral features in this wavelength range that can be used to constrain their compositions (e.g., R. Hu et al. 2012; E. A. Whittaker et al. 2022; M. Hammond et al. 2025; K. Paragas et al. 2025). For example, the surface SiO_2 content can be inferred by measuring the location of the MIR Christiansen feature (CF; J. E. Conel 1969) and the corresponding Si–O stretching feature (J. W. Salisbury 1993). The surface compositions of these planets in turn constrain their interior dynamics,

[13] NASA Postdoctoral Fellowship through Oak Ridge Associated Universities.

Original content from this work may be used under the terms of the Creative Commons Attribution 4.0 licence. Any further distribution of this work must maintain attribution to the author(s) and the title of the work, journal citation and DOI.

Table 1
Summary of JWST Observations of LHS 3844 b Analyzed in This Work

Visit	JWST Obs. #	Date (UT)	Start (UT)	End (UT)	skip_emicorr	spec_hw	bg_hw	Fit Parameters
GO 1846 #1	1	2023 Jun 19	02:52:07	06:06:27	False	3	10	c_0, c_1, r_0, r_1, $c_{\rm xpos}$, $c_{\rm ypos}$
GO 1846 #2	102	2023 Sep 30	08:15:59	11:55:36	False	3	12	c_0, r_0, r_1, $c_{\rm ypos}$, $c_{\rm ywidth}$
GO 1846 #3	3	2024 May 3	23:04:50	03:06:08	False	2	16	c_0, r_0, r_1, $c_{\rm xpos}$, $c_{\rm ypos}$, $c_{\rm xwidth}$, $c_{\rm ywidth}$
GO 7953 #1	6	2025 Jul 10	07:22:35	11:59:55	True	5	8	c_0, c_1, r_0, r_1, $c_{\rm ypos}$, $c_{\rm xwidth}$, $c_{\rm ywidth}$
GO 7953 #2	3	2025 Aug 16	08:12:10	12:49:23	False	5	8	c_0, r_0, r_1, $c_{\rm ypos}$, $c_{\rm ywidth}$
GO 7953 #3	2	2025 Sep 29	19:43:48	23:41:31	False	4	8	c_0, r_0, r_1, $c_{\rm xpos}$, $c_{\rm ypos}$, $c_{\rm xwidth}$, $c_{\rm ywidth}$
GO 7953 #4	4	2025 Sep 30	06:29:41	10:33:48	False	3	12	c_0, r_0, r_1, $c_{\rm ypos}$, $c_{\rm xwidth}$
GO 7953 #5	5	2025 Oct 1	16:01:40	19:53:43	False	2	6	c_0, c_1, r_0, r_1, $c_{\rm xpos}$
GO 7953 #6	7	2025 Oct 2	02:41:24	07:00:31	False	3	20	c_0, r_0, r_1, $c_{\rm xpos}$, $c_{\rm ypos}$, $c_{\rm xwidth}$
GO 7953 #7	8	2025 Oct 3	00:58:42	05:13:55	False	6	6	c_0, c_1, r_0, r_1, $c_{\rm ypos}$, $c_{\rm xwidth}$, $c_{\rm ywidth}$
GO 7953 #8	1	2025 Oct 16	23:42:55	04:20:11	False	4	12	c_0, c_1, r_0, r_1, $c_{\rm xpos}$, $c_{\rm ypos}$, $c_{\rm xwidth}$

Note. The fit parameters are described in the light-curve modeling subsection in Section 2.

including the depth and vigor of mantle convection, which has implications for crustal recycling rates (see review by C. M. Guimond et al. 2024, and references therein). In a separate dimension of characterization, older planetary surfaces will be particulate in nature, due to the effects of ongoing meteorite impacts, while newer surfaces will contain much larger slabs of solid, rocky material. These two surface types can be differentiated by the strength of the transparency feature, which is created by multiple scattering in powdered materials and single scattering in rock slabs (e.g., K. Paragas et al. 2025). At the same time, the retrieved dayside temperature can be used to infer the planet's surface albedo, which is sensitive to the composition, particle size, and amount of space weathering (e.g., X. Lyu et al. 2024; B. P. Coy et al. 2025). This means that emission spectroscopy of airless rocky exoplanets with solid (i.e., not molten) dayside surfaces offers a rich window into their surface properties and corresponding geological histories.

Among this set of planets, LHS 3844 b stands out as the most favorable target for surface characterization. With a radius of $R_{\rm p} = 1.303 \pm 0.022\,R_{\oplus}$ and a mass of $M_{\rm p} = 2.27 \pm 0.23\,M_{\oplus}$ (R. Vanderspek et al. 2019; A. Hacker et al. 2026; E. Nagel et al. 2026), its average density is consistent with an Earth-like bulk composition. Although it has an orbital period of just 11.1 hr, it still has a relatively low equilibrium temperature of $T_{\rm eq} = 816$ K thanks to the small radius ($R_{*} = 0.189\,R_{\odot}$) and low effective temperature ($T_{\rm eff} = 3080$ K) of its mid M dwarf host (R. Vanderspek et al. 2019; E. Nagel et al. 2026). This low equilibrium temperature corresponds to a maximum predicted dayside temperature of 1045 K at the substellar point for the zero-albedo case, below the melting point of most silicates.

Published observations of LHS 3844 b place strict upper limits on the thickness of its atmosphere, indicating that its thermal emission spectrum should be dominated by surface features. L. Kreidberg et al. (2019) used the Spitzer Space Telescope (Spitzer) to measure LHS 3844 b's infrared phase curve in the 4.5 μm bandpass and concluded that its large day–night brightness temperature difference is best matched by atmosphere models with surface pressures less than 0.1 bar. Follow-up ground-based transmission spectroscopy of the planet was consistent with a flat line and ruled out atmospheric scenarios with pressures greater than 0.1 bar (H. Diamond-Lowe et al. 2020). More recently, S. Zieba et al. (2026) measured its MIR dayside emission spectrum with MIRI in Low Resolution Spectroscopy (LRS) mode and found that it is consistent with a blackbody, with no detected spectral features. This study placed even tighter upper limits of 100 mbar (5σ) and 10 μbar (3σ) surface pressures for atmospheres with trace concentrations of CO_2 and SO_2, respectively. Although these observations also placed tight constraints on the planet's dayside Bond albedo, they did not detect any statistically significant surface spectral features and therefore could be matched by a broad range of surface compositions (S. Zieba et al. 2026).

Here we present an improved JWST/MIRI/LRS emission spectrum for LHS 3844 b constructed from a total of 11 secondary eclipses, including the three published eclipses from S. Zieba et al. (2026) and eight new eclipses from GO 7953 (PI: K. Paragas). In Section 2 we describe our analysis of the JWST observations including both the planetary and stellar MIR emission spectra. In Section 3.1, we fit LHS 3844 b's measured emission spectrum with a blackbody, report a tentative detection of a feature centered at 11.6 μm, and consider whether the feature might be caused by instrumental effects. In Section 4.2, we present surface spectral models motivated by the tentative feature, show that the measured spectrum disfavors fine-grained powder materials, and place albedo constraints based on surface material. In Section 5, we discuss the implications of our results for its surface properties as well as provide recommendations for future observational approaches that can improve the quality of the derived spectra and enable refined interpretations of the planet's surface composition.

2. Methods

2.1. Observations

We analyzed 11 secondary eclipse observations of LHS 3844 b taken with the MIRI instrument in the LRS (slitless) mode on board JWST. These observations include three eclipses from Program GO 1846 that were previously published in S. Zieba et al. (2026) and eight new eclipses from Program GO 7953. More information on each individual observation can be found in Table 1. Observations from both programs were obtained using 30 groups per integration, but we increased the overall observing time in the new visits from 2.58 hr (1887 integrations) to 2.84 hr (2225 integrations) in order to allow for better modeling of the exponential ramp at the beginning of each observation. See K. M. Pontoppidan et al. (2016) for detailed explanations of the exposure configuration.

2.2. Data Reduction with Eureka!

We used Eureka! (T. Bell et al. 2022) version 1.3 with jwst pipeline version 1.18.0 and crds version 13.0.6. for Stages 1 through 4, which include detector processing, data calibration, data reduction, and light-curve generation, respectively. For Stage 1, we used the default settings except for jump_rejection_threshold, skip_emicorr, and skip_rcsd. As recommended for time-series observations (TSO) data, we increased the jump_rejection_threshold to 7. We tested True and False settings of both skip_emicorr, a step that corrects for electromagnetic interference (EMI) noise in the raw data when set to False, and skip_rcsd, a step that flags groups that are affected by nonlinear transients that may occur from exponential settling of the detector when set to False. We kept the configuration settings that minimized the median absolute deviation (MAD) in the white light curves. All visits preferred skip_rcsd = True. For Stage 2, we set skip_photom to True as recommended by Eureka! and used the default settings for the remaining parameters. For Stage 3, we used the same values for every MIRI/LRS eclipse. We defined ywindow and xwindow as [109, 388] and [11, 62], respectively. We set ff_outlier to True and bg_thresh to [np.inf, np.inf]. We tested a number of combinations for the background and spectral apertures (bg_hw and spec_hw, respectively), and selected the combination that minimized the MAD in the white light-curve residuals. The values for the other background and spectral extraction parameters can be found in Table 1. For Stage 4, we generated white light curves that span 5.06 to 12.368 μm, and divided each into 12 spectroscopic channels to generate the spectroscopic light curves. We followed the same approach as S. Zieba et al. (2026) for removing outliers by clipping binned data that deviate by more than 4σ using a 20 integration wide box-car filter. We discarded less than 0.5% of integrations for each visit.

2.3. Light-curve Modeling

We used Markov Chain Monte Carlo (MCMC) with emcee (D. Foreman-Mackey et al. 2013) to fit the white light curves for each secondary eclipse with a batman (L. Kreidberg 2015) eclipse model combined with a sinusoidal phase curve model and a systematics model. For the eclipse model, we fixed the orbital period $P = 0.462929709$ days, inclination $i = 89°$, the ratio of the planetary semimajor axis to the stellar radius $a/R_* = 7.122$, and the planet-to-star radius ratio $R_p/R_* = 0.06262$ to the values reported in E. Nagel et al. (2026). We assumed a circular orbit and allowed the eclipse center time t_0 and depth f_p/f_* to vary as free parameters for each individual eclipse observation. For the phase curve model, we use a first order cosine (simple) model $F_{pc,1} = 1 + A_1/2(\cos\phi - 1)$, where F_{pc} is the phase curve flux, A_1 is the phase curve amplitude, and ϕ is given by $\phi = 2\pi(t - t_{sec})/P$ with t_{sec} being the secondary eclipse time. We found that the data do not meaningfully constrain the phase curve amplitude A_1 in our individual eclipse fits. We therefore chose to fix it to one (corresponding to the case of zero emission from the planet's nightside, as expected for an airless planet with no internal heat sources), similar to S. Zieba et al. (2026). We modeled scenarios where the nightside flux was nonzero, and even with a nightside temperature of 500 K, the largest difference from the zero nightside flux case is 12 ppm, less than what could be detectable with our data, over the phase range of our observations. Additionally, we fit the data assuming a first and second order cosine phase curve model using $F_{pc,2} = 1 + A_1/2(\cos\phi - 1) + A_2/2(\cos(2\phi) - 1)$, where A_2 is the amplitude of a secondary cosine term, and we fixed A_1 and A_2 to best-fit values from the NIRSpec phase curve of the planet (S. Zieba et al. 2026, in preparation). The resulting averaged spectrum is consistent with the simple phase curve model $F_{pc,1}(A_1 = 1)$ case, but it is worth noting that the eclipse depths are consistently shallower by about 10 ppm until 10 μm and then deeper at the two longest-wavelength bins at 11.5 and 12 μm compared to the averaged spectrum assuming the simple phase curve model.

Our initial systematics model for each eclipse included a linear trend (c_0 and c_1 as the constant and slope, respectively), an exponential ramp (r_0 and r_1 as the amplitude and decay constant, respectively), and linear coefficients for the measured pointing drift and changes in the point-spread function width in both the x- and y-directions, and the dispersion and spatial directions (c_{xpos}, c_{ypos}, c_{xwidth}, and c_{ywidth}). For each observation, we decided which components, except for the constant trend c_0 which is used universally, of this instrumental model to include by minimizing the Bayesian information criterion (BIC; G. Schwarz 1978). For cases where the difference between the best and second-best models was a statistical wash (ΔBIC < 3), we picked the model with fewer free parameters. The resulting white light curves and best-fit model are shown in Figure 1. The fit parameters used for each observation are listed in Table 1.

To assess the quality of our white light-curve fits, we calculated the rms of the residuals as a function of bin size from zero (unbinned data) to 207 bins ($\sim$10% of the data in each bin) to create time-averaging plots and compared this to the expected noise scaling of $\sqrt{n_{bins}}$ (F. Pont et al. 2006). We found that most observations were well behaved, with minimal evidence for correlated noise. However, there were two observations that had some excess noise on longer timescales. The observation taken on 2025 September 29 has a few upticks in flux that occurred 12, 84, and 149 minutes into our observation. The last uptick coincided with the end of egress and may be a flare. The observation taken on 2025 October 3 has a residual structure that spans 60951.141 to 60951.192 $BMJD_{TDB}$ with consistently low flux values. Although a qualitatively similar structure appeared in the y-centroid time series, this feature did not vanish when we included this parameter as a detrending vector in our fit. Despite these issues, we found that the dayside emission spectra from these two visits were in good agreement with the other nine visits, and therefore included them in our averaged dayside emission spectrum.

For the spectroscopic light-curve fits, we followed S. Zieba et al. (2026) by binning the data into 12 channels between 5.06 to 12.368 μm, each with a width of 0.609 μm. We fit the resulting light curves in each channel with the same set of parameters as the white light curves except for the transit time t_0, which we fixed to the best-fit value from the white light-curve fit. We then took the inverse-variance-weighted average of the 11 individual eclipse depths in each bandpass to construct the averaged emission spectrum (Figure 2). We found that this spectrum is consistent with the published spectrum from S. Zieba et al. (2026) using the first three eclipse observations, which we plot for comparison.

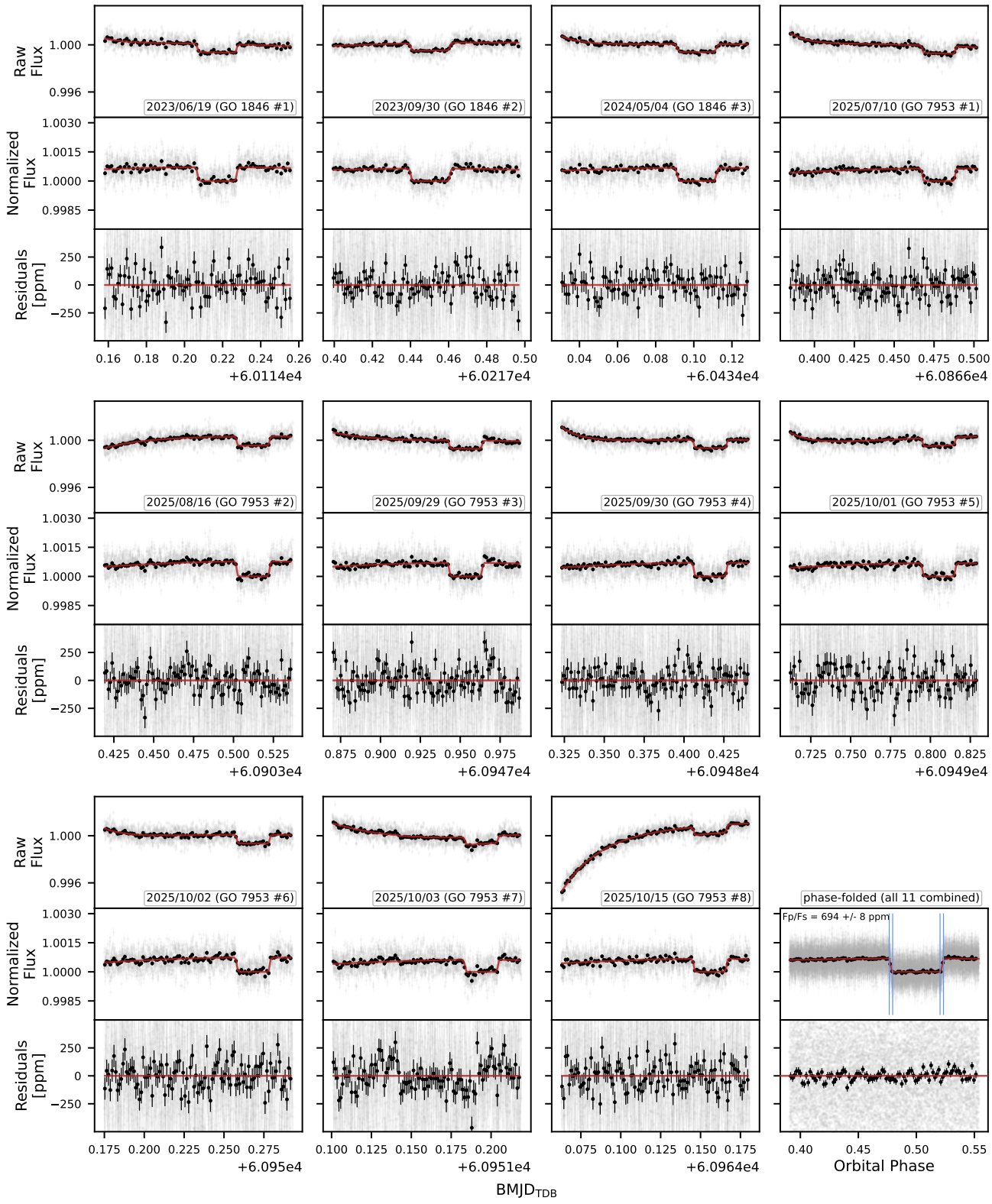


Figure 1. The 11 three-panel plots show the raw flux, normalized flux, and residuals of the white light curves for each MIRI/LRS eclipse with their best-fit model overplotted in red. The two-panel figure in the bottom right is the phase-folded combined white light curve of all 11 visits with the blue vertical lines indicating T1–T4, i.e., ingress and egress. The gray points are the raw data at the native resolution of the observations while the black points are the binned data to a cadence of 1.6 minutes. (The data used to create this figure are available in the online article.)

2.4. Stellar Spectrum

In order to predict the wavelength-dependent secondary eclipse depth for a given planetary surface model, we must divide the predicted planetary emission spectrum by the stellar spectrum. We used `Eureka!` following the process detailed in S. Zieba et al. (2026) to estimate the stellar flux in physical units during each of our 11 MIRI/LRS observations and then

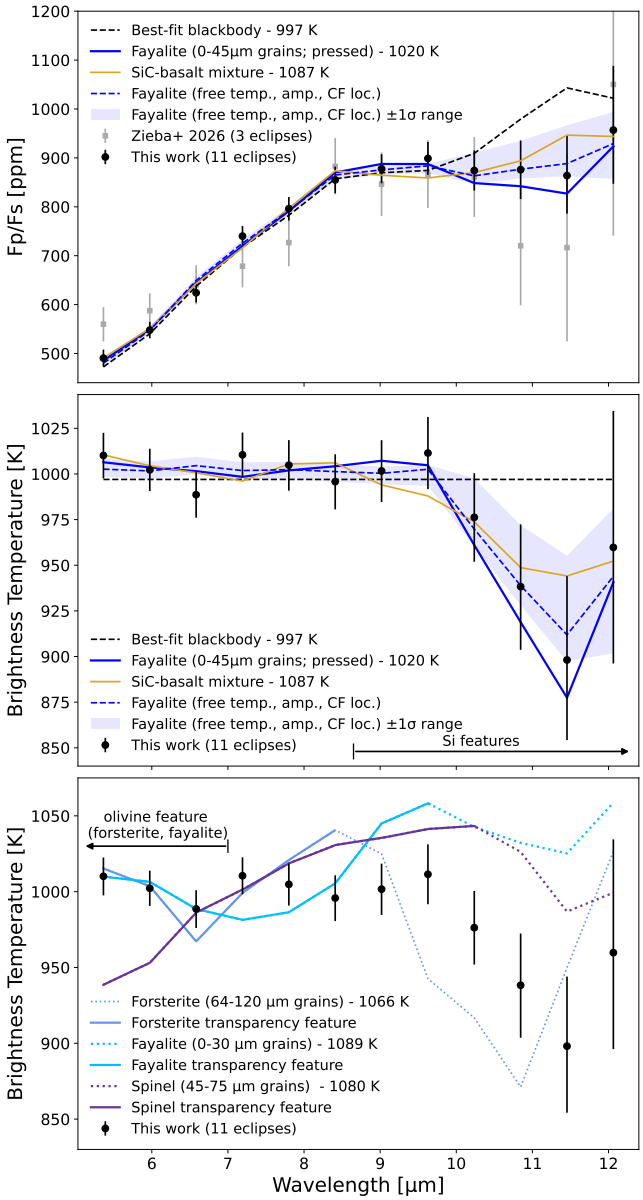


Figure 2. Top: planet-to-star flux ratio emission spectrum from the three eclipses published in S. Zieba et al. (2026), compared to the combined spectrum from all 11 eclipses in this work (including the three previously published). Middle and bottom: the same spectrum converted to brightness temperature to highlight the feature near 10–12 μm. The top two panels show the best-fit blackbody, fayalite, and SiC–basalt mixture models (each with temperature as a free parameter), and the three-parameter Fayalite model with temperature ("temp."), amplitude ("amp."), and CF location ("CF loc.") as free parameters. The bottom panel shows the best-fit forsterite, fayalite, and spinel models of small, loosely packed grains with their corresponding transparency features denoted by the solid lines.

(The data used to create this figure are available in the online article.)

calculated an averaged flux-calibrated stellar spectrum. This is the same approach taken in S. Zieba et al. (2026), and it is motivated by the fact that there can be significant discrepancies between the measured and predicted infrared spectra of M dwarfs similar to LHS 3844 b (T. J. Fauchez et al. 2025).

In Stage 1, the only change we made was to set `skip_emicorr` to `True`. In Stage 2, we set `skip_photom` to `False`. We also increased the target and background aperture sizes to 18 and 19, respectively, to ensure that we captured all of the stellar flux. We only extracted the stellar flux from observations taken during the secondary eclipse (i.e., when the planet was behind the star, between second and third points of contact; see Figure 1) to ensure that the planet's thermal emission did not contaminate the stellar spectrum. We checked for variability in the total stellar flux between observational epochs by integrating each spectrum across the 5.06 to 12.368 μm. We found that the observation taken on 2023 June 19 (GO 1846 #1) has the lowest flux at $9.6577 \times 10^4\,\mathrm{W\,m^{-2}}$ and the observation taken on 2025 October 3 (GO 7953 #7) has the highest flux at $9.8954 \times 10^4\,\mathrm{W\,m^{-2}}$. This 2.4% difference is comparable to the few-percent uncertainty in JWST's absolute flux calibration (D. R. Law et al. 2025). We also confirmed that using either the lowest or highest observed stellar spectrum in our calculations resulted in a negligible change in the predicted secondary eclipse depths. We therefore took the weighted mean of the 11 spectra and adopted this as the empirical stellar spectrum for our model fits.

In our fits, it is also sometimes useful to calculate a predicted dayside equilibrium temperature using a stellar spectrum that spans the full optical to infrared wavelength range. This is required in order to constrain the planetary albedo. We do not have an empirically measured stellar spectrum spanning the required wavelengths, so we instead used a SPHINX stellar spectral model for this purpose. We calculated this model using updated values for the stellar effective temperature $T_{\rm eff} = 3080 \pm 50$ K and metallicity [Fe/H] $= 0.22 \pm 0.10$ dex from E. Nagel et al. (2026). We find that the SPHINX stellar spectrum differs from our empirically measured MIR JWST spectrum by up to 15%, similar to what was presented in S. Zieba et al. (2026).

3. Blackbody Fit and Feature Significance

3.1. Blackbody Fits

In order to determine the extent to which the observed spectrum is consistent with a blackbody function, we converted our wavelength-dependent secondary eclipse measurements into wavelength-dependent brightness temperatures (Figure 2). We found that LHS 3844 b has an effectively constant brightness temperature from 5 to 10 μm, with a dip longward of 10 μm. We fit the full spectrum with a two-parameter model where surface temperature and $R_{\rm p}/R_*$ were allowed to vary in the fit in order to incorporate relevant uncertainties in the latter. We placed a uniform prior of $\mathcal{U}(900, 1200)$ K on the blackbody temperature and a Gaussian prior of $\mathcal{N}(0.6262, 0.00073)$ on $R_{\rm p}/R_*$ based on the value reported in E. Nagel et al. (2026). This resulted in a best-fit blackbody temperature of $T = 997 \pm 11$ K ($\log Z = 102.7$; $\chi^2 = 13.2$). This temperature is in good agreement (0.3σ) with the best-fit blackbody temperature of of 1000^{+15}_{-14} K reported in S. Zieba et al. (2026). We used this fitted brightness temperature to calculate an updated estimate of the brightness temperature ratio $\mathcal{R}_{\rm spec} = 0.95 \pm 0.03$, which is defined as the ratio between the measured dayside brightness temperature and the maximum predicted brightness temperature for a planet with an albedo of zero and no energy redistribution (the latter condition, translating into $\mathcal{R}_{\rm spec} = 1$, is the default expectation for an airless body; B. P. Coy et al. 2025). This value remains close to unity, favoring a low dayside albedo, $A_{\rm B} = 0.16 \pm 0.07$, and a low day–night redistribution efficiency for this planet.

Although the emission spectrum is featureless shortward of $\sim$10 μm, there appears to be a dip in brightness temperature between 10 and 12 μm. S. Zieba et al. (2026) also tentatively noted the presence of a similar feature in their analysis, but concluded that it was not detected at a statistically significant level in their three observations. If the surface of the planet is dominated by silicates, this feature might be an Si–O stretching feature (the strongest diagnostic silicate spectral feature; J. W. Salisbury 1993; R. Hu et al. 2012; K. Paragas et al. 2025). To determine the feature significance, we incorporated a Gaussian feature model into our blackbody fit, which now has three additional free parameters: the amplitude, wavelength center, and width (σ) of the Gaussian function. We placed priors on the Gaussian parameters based on the range of their best-fit values from fitting the Si–O stretching features of all of the solid samples in K. Paragas et al. (2025): $\mathcal{U}(0, 300)$ ppm for the amplitude, $\mathcal{U}(9, 13)$ μm for the wavelength center, and $\mathcal{U}(0, 2.7)$ μm for the width. We used nested sampling with `dynesty` (J. S. Speagle 2020; S. Koposov et al. 2025) to sample the posterior distributions of the free parameters and to estimate the Bayesian evidence Z.

We found that the blackbody and Gaussian fit ($\log Z = 104.9$) resulted in a global best-fit blackbody temperature of 991^{+16}_{-4} K, amplitude of 204^{+35}_{-108} ppm, wavelength center of $11.4^{+1.2}_{-0.1}$ μm, and width of $0.6^{+0.9}_{-0.1}$. The amplitude of the Gaussian feature is greater than zero at 1.9σ significance, and the Bayes factor of $B_{\rm m} = 9.4$ indicates substantial (almost strong) evidence in favor of the model with a Gaussian feature over the pure blackbody model (see Table 1 of D. P. Thorngren et al. 2026).

We fit the same blackbody and Gaussian model to the averaged emission spectrum assuming the best-fit NIRSpec phase curve shape (see Section 2.3; S. Zieba et al. 2026, in preparation), and retrieved a slightly higher temperature of 1012^{+11}_{-10} K and larger amplitude of 266^{+72}_{-76} ppm, which are 1.1σ and 0.5σ consistent, respectively, with our results assuming a simple sinusoidal phase curve model with zero nightside emission. For this case, the fitted Gaussian amplitude for the candidate feature is detected at higher significance (3.5σ), while the best-fit wavelength center and width are both 0.3σ consistent with the previous fit. In this fit, the data prefer the Gaussian model over a blackbody-only model with a Bayes factor $B_{\rm m} = 218$, indicating decisive evidence in favor of the feature. We note that the phase curve model we used in this fit is still preliminary and is based on unpublished data at wavelengths shorter than those spanned by our observations, so we conservatively adopt the simpler physically motivated sinusoidal phase curve model in all of our subsequent analyses moving forward. We note that a Gaussian shape is not a very good approximation of most of the complex and sometimes asymmetric Si–O stretching features in the K. Paragas et al. (2025) spectral library. We therefore refer readers to Section 4.2 below, where we use a more realistic surface model to fit the feature.

3.2. Can the Feature Be Explained by Residual Ramp Effects?

In the previous section, we evaluated the statistical significance of the observed feature assuming independent Gaussian-distributed uncertainties for our wavelength-dependent secondary eclipse depths. However, previous studies have shown that MIRI/LRS measurements frequently exhibit a sudden change in ramp shape for bins longward of 10.5 μm, known as the shadowed region effect (T. Bell et al. 2022). Although there are not any obvious covariances between our retrieved eclipse depths and the exponential ramp coefficients in our fit, previous studies (e.g., E. Agol et al. 2010) have shown that exponential ramps can subtly bias the retrieved eclipse depths. Although the underlying cause of the change in ramp shape at longer wavelengths is still under investigation, it is thought to be caused by uneven illumination of the subarray in the preceding observation. Because it depends on the previous illumination history of the array, it is not consistently present in all MIRI/LRS observations.

We examined our observations and found that there is a change in ramp shape longward of 10 μm in several visits. An example of this behavior is shown in panel (a) of Figure 3, in which the spectral channels shortward of 10 μm have positive ramp amplitudes while the ones longward of 10 μm have negative ramp amplitudes that invert the shape of the ramps from decreasing to increasing with time. We investigated whether this change in ramp shape might produce the long-wavelength feature in our emission spectrum by plotting the amplitude of the exponential ramp r_0 and corresponding secondary eclipse depth in the 10.8 μm bin for each of our 11 individual observations (Figure 3 (b)). We then subdivided the data into a set of five observations with stronger ramps (2023 June 19, GO 1846 #1; 2024 May 4, GO 1846 #3; 2025 June 16, GO 7953 #2; 2025 October 1, GO 7953 #5; and 2025 October 16, GO 7953 #8) and six observations with weaker ramps, and calculated an averaged emission spectrum for each group (bottom two panels of Figure 3). We then jointly fit the two emission spectra with the same blackbody and Gaussian feature model discussed in Section 3.1, where we allowed the temperature and amplitude to vary between the two spectra but assumed a shared wavelength center and feature width.

We retrieved an amplitude of 210^{+34}_{-97} ppm (2.2σ) for the spectrum generated from the observations with more negative ramp amplitudes (corresponding to increasing flux with time) and an amplitude of 79^{+112}_{-45} ppm (1.8σ) for the spectrum generated from the observations with shallower ramp amplitudes. As expected, our retrieved surface temperatures, wavelength center, and feature width were all consistent with our previous fit to the full dataset. Although the observations with more negative ramps appear to have a larger feature amplitude, the two retrieved amplitudes only differ by 0.4σ. Additionally, we calculated the Pearson correlation coefficient between the secondary eclipse depths and amplitudes of the exponential ramps in the 10.8 μm bin, and found a value of 0.47 with a 95% confidence interval range of –0.18 to 0.83, indicating a relatively weak correlation.

Next, we created another averaged spectrum, excluding the three observations with the strongest shadowed region effects (i.e., the three observations with the most negative r_0 in panel (b) of Figure 3). We fit this spectrum with the same blackbody and Gaussian model, and retrieved an amplitude of 315^{+48}_{-57} (5.5σ), suggesting that the observations that are the most affected by the shadowed region may actually bias the fitted feature amplitude to lower values, weakening its detection significance. We conclude that the current data are too noisy to diagnose whether the observed feature is influenced by the exponential ramp shape.

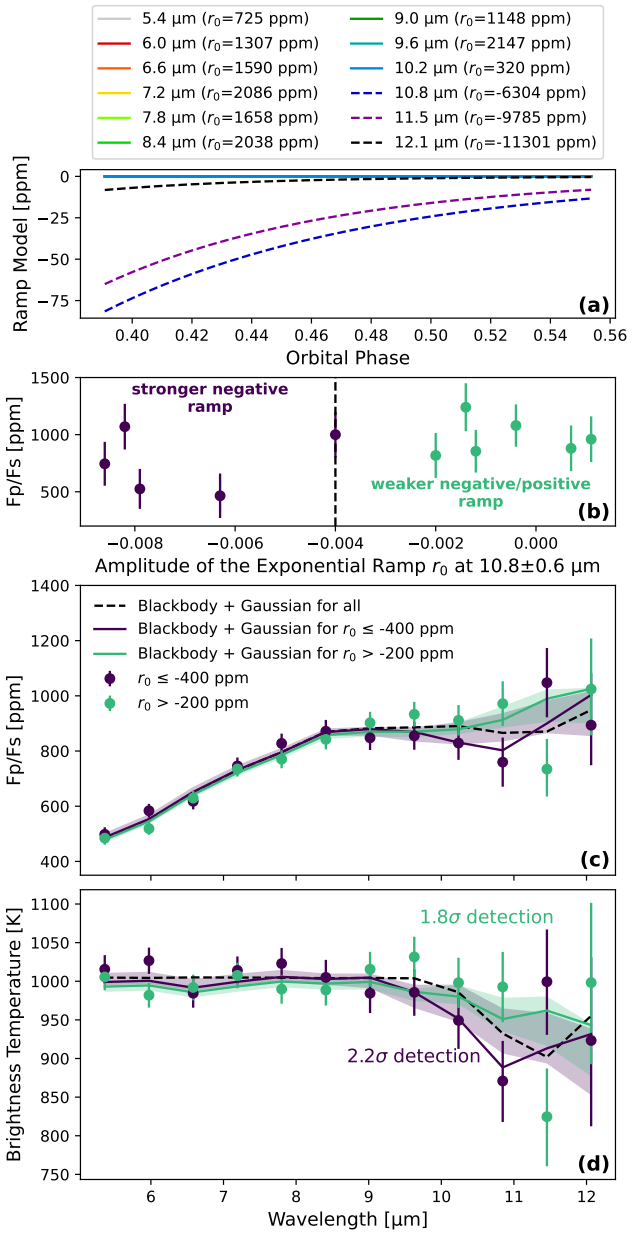


Figure 3. (a) The ramp models for all spectral channels for GO 7953 #5 (2025 October 1) showing the change in ramp shape for channels in the shadowed region. (b) The planet-to-star flux ratios of each observation as a function of the ramp amplitude r_0 in the 10.8(6) μm bin. (c) The averaged planet-to-star flux spectra for the two groups. (d) The same spectra converted to brightness temperature. Panels (c) and (d) include the blackbody and Gaussian feature model (free temperature, amplitude, center, and width) fit to all 11 observations and each subgroup. The shaded regions correspond to the 1σ range of the best-fit models. The feature amplitude is detected to 2.2σ for the stronger ramp amplitude group and 1.8σ for the weaker ramp amplitude group.

4. Bare Rock Surface Models

4.1. Surface Spectral Libraries

If the tentative feature between 10 and 12 μm is astrophysical rather than instrumental in nature, we can identify representative surface compositions that might provide a good match to its measured shape. We modeled the emission spectrum of LHS 3844 b following the approaches in M. Hammond et al. (2025) and K. Paragas et al. (2025). Although we initially considered models based on the surface types from R. Hu et al. (2012) and K. Paragas et al. (2025), we found that none were a good match to our data. We therefore expanded our search into spectral libraries and used the bidirectional reflectance measurements from the RELAB database (R. E. Milliken et al. 2021) to explore a wider variety of potential surface compositions. We followed the steps outlined in M. Hammond et al. (2025) to derive the single scattering albedo ω and the directional-hemispheric reflectance $r_{\rm dh}$ for a given material. We then used those values to calculate the hemispheric emissivity ϵ_h assuming isotropic scattering. This is an important caveat for our model predictions: most surfaces are not isotropic scatterers, but measurements obtained at a single scattering angle, such as those provided in RELAB, do not independently constrain the full angular scattering behavior of the samples needed to convert them into disk-integrated planetary spectra (e.g., C. Pilorget et al. 2016; L. Gkouvelis 2025a). However, these simplifying assumptions are sufficient for our purpose here, which is to identify simple end-member surface compositions that might have features in the desired wavelength range.

After calculating the hemispheric emissivity, we followed the steps in K. Paragas et al. (2025) to calculate the outgoing planetary flux. For each surface type, we also derived the 1D correction factor f. This factor is calculated by comparing our 1D surface model to the output of a 3D surface model from R. Hu et al. (2012) that calculates the equilibrium temperature at every point on the planet.

4.2. Surface Composition

In principle we can calculate a predicted equilibrium surface temperature and corresponding dayside emission spectrum for each of these materials using their measured reflectances (e.g., R. Hu et al. 2012; K. Paragas et al. 2025; S. Zieba et al. 2026). However, if the planetary surface includes a mixture of several materials, this can result in a wide range of optical albedos while preserving infrared spectral features from individual mineral constituents. Similarly, space weathering from micrometeoroid bombardment and/or excess irradiation (e.g., solar wind and cosmic rays; C. M. Pieters & S. K. Noble 2016; X. Lyu et al. 2024) can systematically darken older surfaces on airless planetary bodies, increasing their corresponding equilibrium dayside temperatures. Particle size also exerts substantial control on albedo (C. M. Pieters 1983). We therefore allowed the dayside temperature to vary as a free parameter in our fit.

The CF is an emissivity maximum in the spectrum. In silicates, it is located at the beginning of the Si–O stretching feature, and its wavelength position is correlated with the SiO_2 weight percent of the material (J. E. Conel 1969). This effect can be measured in spectrally coarse-resolution data of planetary surfaces (T. D. Glotch et al. 2010). Specifically, if particle size and surface temperature gradient are constant, the CF peak occurs at longer wavelengths for lower SiO_2 weight percent and at shorter wavelengths for greater SiO_2 weight percent. Particle size, particle packing, and surface temperature gradients also influence the position (L. M. Logan et al. 1973; K. L. Donaldson Hanna et al. 2012). In order to match the relatively long wavelength of the candidate CF observed in our data, near 10 μm, as well as the brightness temperature minimum near 11.5 μm we selected materials with features that occur at similar wavelengths, including olivine iron and magnesium end-members fayalite and forsterite, respectively,

spinels (found in primitive solar system materials and some igneous rocks; e.g., T. H. Burbine et al. 1992; J. M. Sunshine et al. 2008), and SiC (a possible exotic composition for rocky exoplanets; C. M. Guimond et al. 2024, and references therein) from the RELAB database. We selected these materials to demonstrate that there are multiple candidate surface compositions that may be able to match the long-wavelength feature in our observations.

For each surface type considered, we identified samples in RELAB with a range of grain sizes and/or packing methods. We considered two olivines, fayalite and forsterite. We found that the fayalite sample (ID: DD-MDD-098-P; 0–45 μm grains that have been pressed into a pellet) provided the best overall fit ($\chi^2 = 3.6$ for 12 data points and two free parameters, temperature and the ratio of the planet-to-stellar radii) with a retrieved temperature of 1020^{+12}_{-11} K. This χ^2 is significantly lower than the χ^2 value of the blackbody-only fit of 12.9, indicating an improvement in fit quality. Although it is also lower than $\chi^2_\nu \approx 1$, where $\chi^2_\nu = \chi^2/\nu$ and $\nu = n - m$ with n being the number of data points and m being the number of free parameters, this is not surprising given the large number of available materials in RELAB, which collectively span a wide range of spectral feature depths, widths, and locations.

This specific fayalite powder sample was pressed into a pellet, making its spectrum more closely resemble that of a solid slab than a loosely packed powder sample (J. W. Salisbury et al. 1987), effectively eliminating the transparency feature (e.g., K. Paragas et al. 2025). To determine whether or not we see evidence for the transparency feature, we also fit a model using the fayalite sample (ID: DH-MBW-006) with loosely packed 0–30 μm grains. This sample was disfavored ($\chi^2 = 40.8$; 1089 ± 13 K) by the data due to the combination of the rising slope between 7 and 10 μm and the shallower Si–O stretching feature caused by the transparency feature (see the bottom panel of Figure 2). None of the forsterite samples were able to match the observed location of the candidate CF in our observations, resulting in a lower quality fit ($\chi^2 = 39.8$; 1066 ± 12 K) for our preferred sample (ID: DH-MBW-009; 64–120 μm grains). We note that the available forsterite samples were also loosely packed powders, and therefore displayed a transparency feature that was also disfavored by our data.

Spinel has been found in early formed materials, such as calcium aluminum inclusions (e.g., J. M. Sunshine et al. 2008), >4 Ga old asteroids (e.g., T. H. Burbine et al. 1992), and in assemblages with mafic to ultramafic rocks on the Moon (e.g., C. M. Pieters et al. 2011). It also has an emissivity minimum feature at wavelengths similar to the one in our data. However, the spinels available in RELAB were limited to loosely packed powder samples with very strong transparency features. We selected one ($\chi^2 = 99.2$; ID: SP-CMP-077-C; 45–75 μm grains) to show as an example in Figure 2. We found that this spinel exhibits a feature around 11 μm that is a potential compositional match, but the loosely packed particle texture characteristic of this particular RELAB sample is disfavored due to the presence of a strong transparency feature that manifests in the spectrum as a steep slope between 5 and 10.3 μm. In the future, additional lab measurements of larger grained and/or pressed spinel samples could provide an improved fit to our observations.

We also found that silicon carbide, SiC, surface models provided a reasonable match to our data. SiC has been suggested as a possible exotic composition for rocky exoplanets that have formed in high-C/O environments (K. Hakim et al. 2018, 2019; F. Miozzi et al. 2018; H. Allen-Sutter et al. 2020; C. M. Guimond et al. 2024), and observed as dust around carbon-rich stars (A. K. Speck et al. 2009; G. C. Sloan et al. 2014). There was only one SiC sample (ID: MM-PTB-001; a silicon carbide slab) available in RELAB with sufficient MIR wavelength coverage. Although this sample has an absorption feature at a wavelength similar to that observed in our data, the SiC feature in our best-fit surface model is far too deep ($\chi^2 = 313.1$). We therefore considered a linear mixture of the SiC sample and the K1919 basalt powder from K. Paragas et al. (2025), which we chose, not for geological plausibility, but solely because it is a dark and relatively featureless material. We found that a mixture of 63% SiC and 37% K1919 basalt powder provides a better fit to the data ($\chi^2 = 5.6$; 1087 ± 14 K). The best-fit models for all surface types considered are shown in Figure 2.

Both laboratory and theoretical studies have shown that the depths of surface spectral features seen in emission are sensitive to the unknown near-surface temperature gradient (e.g., K. L. Donaldson Hanna et al. 2012; K. Paragas et al. 2025; X. Lyu & D. D. B. Koll 2026). We therefore repeated our fit for the fayalite surface model, but this time we allowed the depth of the Si–O stretching feature to vary as a free parameter in the fit. We also allowed the location of the feature to vary in the fit, allowing us to obtain a corresponding constraint on the location of the CF. For this test, we modeled the surface as a blackbody with the fayalite Si–O stretching feature superimposed onto it. We used nested sampling with `dynesty` to sample the posterior distributions of the blackbody temperature, the depth of the Si–O stretching feature, and the CF wavelength (from now on called the "three-parameter model"). We set broad prior ranges of $\mathcal{U}(900, 1200)$ K for the blackbody temperature, $\mathcal{U}(0, 300)$ ppm for the Si–O stretching feature depth, $\mathcal{U}(5, 12)$ μm for the CF wavelength, and a Gaussian prior of $\mathcal{N}(0.6262, 0.00073)$ on R_p/R_* based on E. Nagel et al. (2026). For this three-parameter model, assuming literature values for system parameters, we retrieved a temperature of 996 ± 10 K, an Si–O stretching feature depth of 188^{+61}_{-67} ppm, and a CF wavelength of $10.0^{+0.4}_{-0.3}$ μm.

4.3. Constraints on Surface Albedo from Energy Balance

For each of the surface types considered above, the planet's measured dayside flux implicitly constrains its optical and NIR albedo. Composition, grain size, packing, and space weathering all influence albedo, and its value therefore provides an independent constraint on the planet's dayside surface properties. We quantified this constraint by creating a grid of 3D equilibrium surface models for each surface type using the model framework from R. Hu et al. (2012) with varying Bond albedos A_B. At each grid point, we rescaled the incident flux absorbed by the surface using a scale factor of $(1 - A_{B,new})/(1 - A_{B,orig})$ where $A_{B,new}$ is the new assumed Bond albedo and $A_{B,orig}$ is the original Bond albedo for that surface type. This ensured that we correctly accounted for the changing 3D dayside temperature distribution as we varied A_B. We also accounted for uncertainties in T_* and a/R_* by randomly sampling from Gaussian distributions set by values in E. Nagel et al. (2026) of $\mathcal{N}(3080, 50)$ K and $\mathcal{N}(7.122, 0.078)$, respectively. For the fayalite sample, we retrieved a Bond albedo of 0.18 ± 0.10. This is in good agreement with its true Bond

albedo of 0.17, which we calculated using our SPHINX stellar spectrum and the measured optical to NIR reflectivity of the fayalite sample.

For the SiC and basalt mixture, we retrieved a Bond albedo of 0.08 ± 0.05, which is 3σ less than its true Bond albedo of 0.23. This surface has lower emissivities between 5 and 10 μm than the fayalite sample, and therefore requires higher surface temperatures to match our measured flux. This lower albedo might plausibly be explained by space weathering (e.g., X. Lyu et al. 2024). However, there may also be other grain sizes, packing, or compositional mixtures including this material that can match the observed long-wavelength feature while simultaneously allowing for a lower dayside temperature. Angle-dependent effects, such as the opposition surge, that we neglected in our simplified modeling framework could also result in a higher predicted dayside flux for the same underlying surface composition and temperature (e.g., L. Gkouvelis 2025b).

5. Conclusions

We present an updated MIRI/LRS eclipse spectrum of LHS 3844 b by combining 11 (eight new and three archival) eclipse observations. The data are well matched by a 996 ± 5 K blackbody shortward of 10 μm, and display a tentatively identified feature ($1.9\sigma-3.5\sigma$) between 10 and 12 μm. We explore whether this feature might be produced by the ramp shape changes associated with the shadowed region, and are unable to reach a definitive conclusion. If this feature is astrophysical, its depth and location are consistent with ultramafic materials, such as olivine end-members fayalite (iron) and forsterite (magnesium), spinels, or silicon carbide (SiC). The data disfavor the presence of a strong transparency feature, indicating that the surface is unlikely to be predominately comprised of small loosely packed grains. Assuming a blackbody, the inferred Bond albedo is $A_B = 0.16 \pm 0.07$. In the future, we expect that expanded modeling and/or laboratory measurements of a wider range of geologically plausible mixtures may identify additional models that can provide a good match to these observations. The simple model framework that we utilized here could also be improved by a more detailed consideration of angle-dependent scattering effects (e.g., L. Gkouvelis 2025a, 2025b), near-surface temperature gradients (e.g., X. Lyu & D. D. B. Koll 2026), and temperature-dependent changes in the wavelength locations of spectral features (e.g., M.-A. Fortin et al. 2024; K. Paragas et al. 2025), as well as other related phenomena.

Our observations demonstrate that JWST can achieve the MIR sensitivity required to spectroscopically constrain the surface properties of rocky exoplanets. In the future, NIR observations of LHS 3844 b's emission spectrum with NIRSpec (GO 4008, PI: S. Zieba, and GO 7953, PI: K. Paragas) can be used to obtain improved constraints on the strength of the transparency feature, which is strongest between 3 and 8 μm. This feature is caused by multiple scattering and provides a relatively composition-insensitive diagnostic of the surface particle size and texture, which is related to the surface age (K. Paragas et al. 2025). At the same time, new MIRI/LRS observations are needed in order to investigate the possible influence of the instrumental ramp on the observed $10-12$ μm feature and to collect data of sufficient quality to differentiate between compositional models. The new MIRI/LRS subarrays (SLITLESSPRISM_IP and SLITLESSPRISM_IPS), which were added in Cycle 6, will mitigate wavelength-dependent changes in the ramp shape by shifting the location of the subarray away from the shadowed region. Future observers might also consider using the "preflash" strategy first developed for MIR Spitzer time series photometry (e.g., D. Deming 2009; H. A. Knutson et al. 2011). This approach exposes the detector to a bright, diffuse source immediately before the science observations, which effectively eliminates the ramp behavior in most observations.

Acknowledgments

We thank Geoffrey Blake for useful discussions about silicon carbide. This work is based on observations made with the NASA/ESA/CSA James Webb Space Telescope. The data were obtained from the Mikulski Archive for Space Telescopes at the Space Telescope Science Institute, which is operated by the Association of Universities for Research in Astronomy, Inc., under NASA contract NAS 5-03127 for JWST. These observations are associated with GO program 7953. Support for US investigators in program 7593 was provided by NASA through a grant from the Space Telescope Science Institute, which is operated by the Association of Universities for Research in Astronomy, Inc., under NASA contract NAS 5-03127. All of the data presented in this article were obtained from the Mikulski Archive for Space Telescopes (MAST) at the Space Telescope Science Institute. The specific observations analyzed can be accessed via DOI: 10.17909/gppv-t130 and DOI: 10.17909/94sq-tr83. The models used in this study were developed at the Jet Propulsion Laboratory and the California Institute of Technology under a contract with the National Aeronautics and Space Administration and funded through the President's and Director's Research & Development Fund Program. S.Z. was supported by NASA through the NASA Hubble Fellowship grant #HST-HF2-51570.001-A awarded by the Space Telescope Science Institute, which is operated by the Association of Universities for Research in Astronomy, Incorporated, under NASA contract NAS 5-26555.

Facility: JWST (MIRI/LRS).

Software: `astropy` (Astropy Collaboration et al. 2013, 2018, 2022), `batman` (L. Kreidberg 2015), `dynesty` (J. S. Speagle 2020; S. Koposov et al. 2025), `emcee` (D. Foreman-Mackey et al. 2013), `Eureka!` (T. Bell et al. 2022).

Appendix A
Individual Visits

As discussed in Section 2, we constructed the average emission spectrum shown in Figure 2 by taking the inverse-weighted average of the 11 individual eclipse depths in each bandpass. The eclipse depth spectrum for each individual observation is shown in Figure A1. We highlight the two visits with the most correlated noise, GO 7953 #3 from 2025 September 29 and GO 7953 #7 from 2025 October 3 by marking them as squares outlined in black. They appear to be consistent with the other visits. We note that for GO 7953 #7, the two longest-wavelength eclipse depths are relatively low, but their uncertainties and the overall scatter among all visits are larger in these bins.

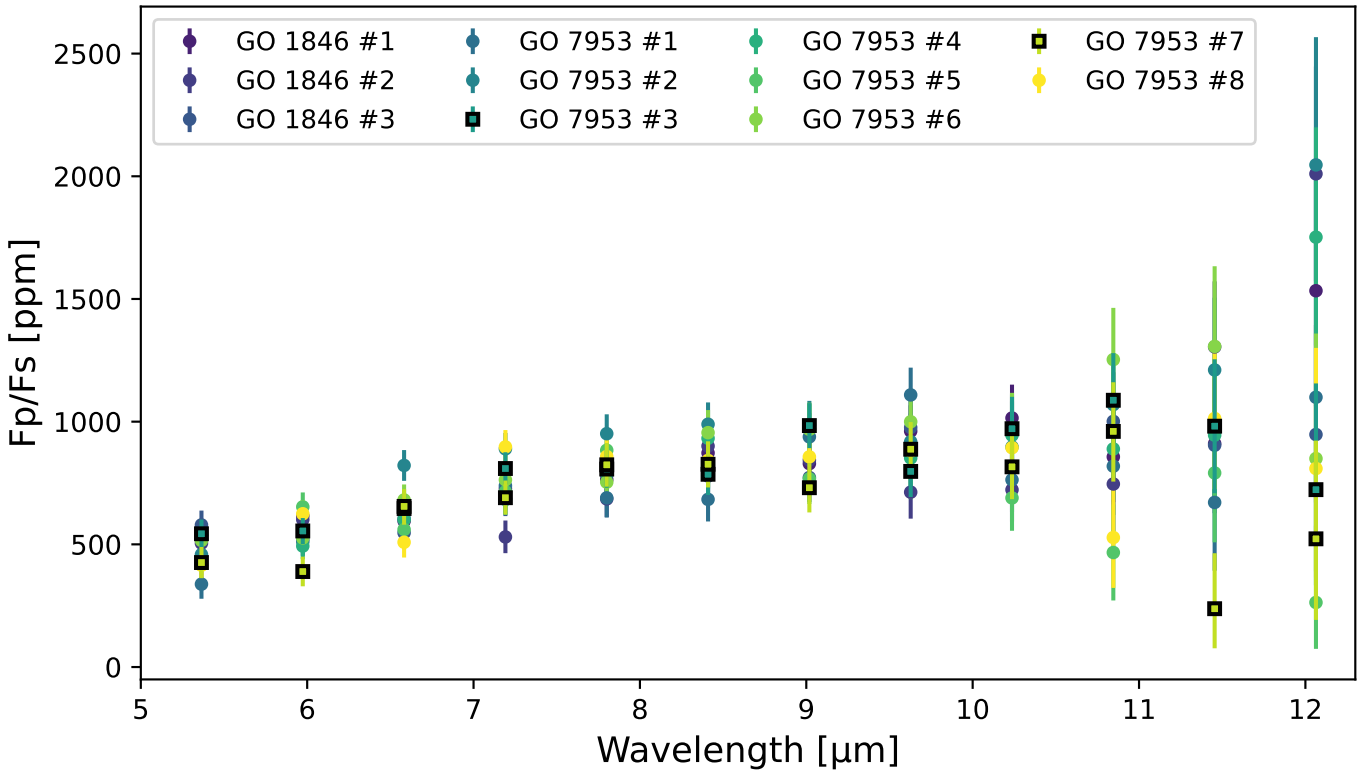


Figure A1. The individual emission spectra of each observation. The two sets of square markers outlined in black are the two visits with excess noise noted in Section 2.

(The data used to create this figure are available in the online article.)

Appendix B
Stellar Spectra

We show the absolute flux-calibrated stellar spectra from each visit in Figure B1 for further comparison aside from the brief discussion in Section 2 on the stellar spectrum. Most of the spectra overlap across the wavelength range except for GO 7953 #7 and #8, whose spectra are lower between ∼6.8 and ∼10.5 μm. Additionally, we note a similar behavior, as first mentioned in S. Zieba et al. (2026), where the SPHINX spectrum overestimates the flux of the star by ∼15%. This further highlights the important of using absolute flux-calibrated spectra for interpreting future datasets (T. J. Fauchez et al. 2025).

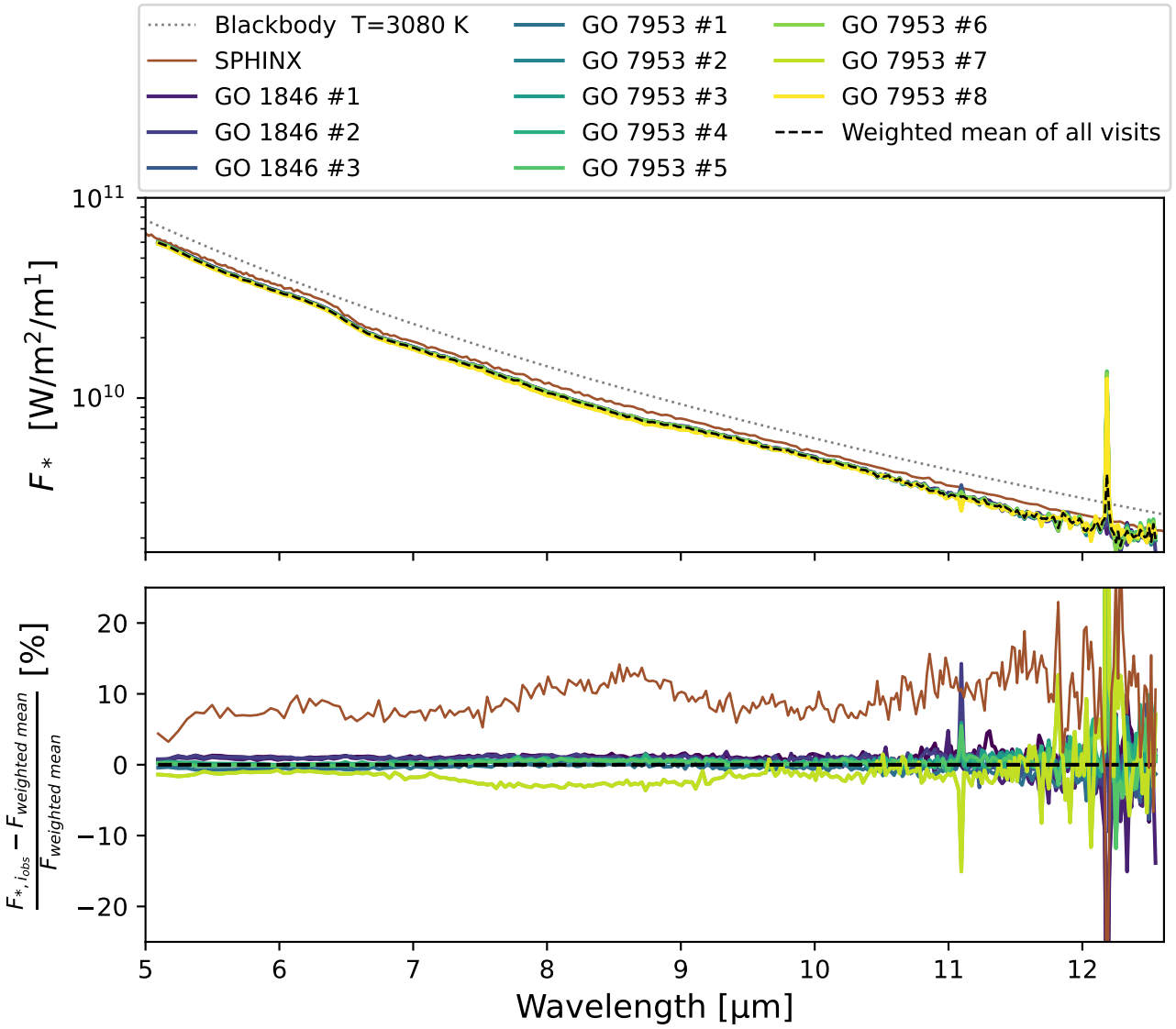


Figure B1. Top: the spectra of a blackbody (3080 K), the SPHINX model, each individual visit, and the weighted mean of all observations. Bottom: the percent difference of each spectra relative to the weighted mean of all visits.
(The data used to create this figure are available in the online article.)

ORCID iDs

Kimberly Paragas https://orcid.org/0000-0003-0062-1168
Heather A. Knutson https://orcid.org/0000-0002-5375-4725
Renyu Hu https://orcid.org/0000-0003-2215-8485
Bethany L. Ehlmann https://orcid.org/0000-0002-2745-3240
Aishwarya R. Iyer https://orcid.org/0000-0003-0971-1709
Sebastian Zieba https://orcid.org/0000-0003-0562-6750
Laura Kreidberg https://orcid.org/0000-0003-0514-1147

References

Agol, E., Cowan, N. B., Knutson, H. A., et al. 2010, ApJ, 721, 1861
Allen, N. H., Espinoza, N., Diamond-Lowe, H., et al. 2025, AJ, 170, 240
Allen-Sutter, H., Garhart, E., Leinenweber, K., et al. 2020, PSJ, 1, 39
Astropy Collaboration, Price-Whelan, A. M., Lim, P. L., et al. 2022, ApJ, 935, 167
Astropy Collaboration, Price-Whelan, A. M., Sipőcz, B. M., et al. 2018, AJ, 156, 123
Astropy Collaboration, Robitaille, T. P., Tollerud, E. J., et al. 2013, A&A, 558, A33
Bell, T., Ahrer, E.-M., Brande, J., et al. 2022, JOSS, 7, 4503
Bello-Arufe, A., Damiano, M., Bennett, K. A., et al. 2025, ApJL, 980, L26
Burbine, T. H., Gaffey, M. J., & Bell, J. F. 1992, Metic, 27, 424
Conel, J. E. 1969, JGR, 74, 1614
Connors, N. J., Monaghan, C., Benneke, B., Dang, L., & Roy, P.-A. 2026, ApJL, 1006, L6
Coy, B. P., Ih, J., Kite, E. S., et al. 2025, ApJ, 987, 22
Coy, B. P., Xue, Q., Weiner Mansfield, M., et al. 2026, ApJL, 1005, L77
Crossfield, I. J. M., Malik, M., Hill, M. L., et al. 2022, ApJL, 937, L17
Deming, D. 2009, IAUS, 253, 197
Diamond-Lowe, H., Charbonneau, D., Malik, M., Kempton, E. M.-R., & Beletsky, Y. 2020, AJ, 160, 188
Donaldson Hanna, K. L., Wyatt, M. B., Thomas, I. R., et al. 2012, JGRE, 117, E00H05
Fauchez, T. J., Ducrot, E., Rackham, B. V., et al. 2025, ApJ, 989, 170
Foreman-Mackey, D., Hogg, D. W., Lang, D., & Goodman, J. 2013, PASP, 125, 306
Fortin, M.-A., Gazel, E., Williams, D. B., et al. 2024, ApJL, 974, L7
Fortune, M., Gibson, N. P., Diamond-Lowe, H., et al. 2025, A&A, 701, A25
Gillon, M., Ducrot, E., Bell, T. J., et al. 2026, NatAs, 10, 674
Gkouvelis, L. 2025a, RNAAS, 9, 320
Gkouvelis, L. 2025b, PSJ, 6, 110
Glotch, T. D., Lucey, P. G., Bandfield, J. L., et al. 2010, Sci, 329, 1510
Greene, T. P., Bell, T. J., Ducrot, E., et al. 2023, Natur, 618, 39

Guimond, C. M., Wang, H., Seidler, F., et al. 2024, RvMG, 90, 259
Hacker, A., Astudillo-Defru, N., Díaz, R. F., et al. 2026, A&A, 710, A312
Hakim, K., Spaargaren, R., Grewal, D. S., et al. 2019, AsBio, 19, 867
Hakim, K., van Westrenen, W., & Dominik, C. 2018, A&A, 618, L6
Hammond, M., Guimond, C. M., Lichtenberg, T., et al. 2025, ApJL, 978, L40
Holmberg, M., Diamond-Lowe, H., Mendonça, J. M., et al. 2026, AJ, 171, 251
Hu, R., Bello-Arufe, A., Zhang, M., et al. 2024, Natur, 630, 609
Hu, R., Ehlmann, B. L., & Seager, S. 2012, ApJ, 752, 7
Knutson, H. A., Madhusudhan, N., Cowan, N. B., et al. 2011, ApJ, 735, 27
Koposov, S., Speagle, J., Barbary, K., et al. 2025, joshspeagle/dynesty: v3.0.0, Zenodo, doi:10.5281/zenodo.17268284
Kreidberg, L. 2015, PASP, 127, 1161
Kreidberg, L., & Stevenson, K. B. 2025, PNAS, 122, e2416190122
Kreidberg, L., Koll, D. D. B., Morley, C., et al. 2019, Natur, 573, 87
Law, D. R., Argyriou, I., Gordon, K. D., et al. 2025, AJ, 169, 67
Logan, L. M., Hunt, G. R., Salisbury, J. W., & Balsamo, S. R. 1973, JGR, 78, 4983
Luque, R., Coy, B. P., Xue, Q., et al. 2025, AJ, 170, 49
Lyu, X., & Koll, D. D. B. 2026, ApJ, 1000, 274
Lyu, X., Koll, D. D. B., Cowan, N. B., et al. 2024, ApJ, 964, 152
Meier Valdés, E. A., Demory, B.-O., Diamond-Lowe, H., et al. 2025, A&A, 698, A68
Milliken, R. E., Hiroi, T., Scholes, D., Slavney, S., & Arvidson, R. 2021, in LPI Contributions, Vol. 2654, Astromaterials Data Management in the Era of Sample-Return Missions Community Workshop, 2021
Miozzi, F., Morard, G., Antonangeli, D., et al. 2018, JGRE, 123, 2295
Monaghan, C., Roy, P.-A., Benneke, B., et al. 2025, AJ, 169, 239
Nagel, E., Köhler, J., Zechmeister, M., et al. 2026, A&A, 710, A311
Paragas, K., Knutson, H. A., Hu, R., et al. 2025, ApJ, 981, 130
Pieters, C. M. 1983, JGR, 88, 9534
Pieters, C. M., & Noble, S. K. 2016, JGRE, 121, 1865
Pieters, C. M., Besse, S., Boardman, J., et al. 2011, JGRE, 116, E00G08
Pilorget, C., Fernando, J., Ehlmann, B. L., Schmidt, F., & Hiroi, T. 2016, Icar, 267, 296
Pont, F., Zucker, S., & Queloz, D. 2006, MNRAS, 373, 231
Pontoppidan, K. M., Pickering, T. E., & Laidler, V. G. 2016, SPIE, 9910, 991016
Rochon, A., Artigau, É., Weisserman, D., et al. 2026, ApJL, 998, L39
Salisbury, J. W. 1993, Cambridge Planetary Science (Cambridge Univ. Press)
Salisbury, J. W., Walter, L., & Vergo, N. 1987, Mid-infrared spectroscopic investigation. NASA TM-89810, NASA 196
Schwarz, G. 1978, AnSta, 6, 461
Sloan, G. C., Lagadec, E., Zijlstra, A. A., et al. 2014, ApJ, 791, 28
Speagle, J. S. 2020, MNRAS, 493, 3132
Speck, A. K., Corman, A. B., Wakeman, K., Wheeler, C. H., & Thompson, G. 2009, ApJ, 691, 1202
Sunshine, J. M., Connolly, H. C., McCoy, T. J., Bus, S. J., & La Croix, L. M. 2008, Sci, 320, 514
Teske, J. K., Wallack, N. L., Piette, A. A. A., et al. 2025, ApJL, 995, L39
Thorngren, D. P., Sing, D. K., & Mukherjee, S. 2026, ApJS, 283, 10
Vanderspek, R., Huang, C. X., Vanderburg, A., et al. 2019, ApJL, 871, L24
Wachiraphan, P., Berta-Thompson, Z. K., Diamond-Lowe, H., et al. 2025, AJ, 169, 311
Weiner Mansfield, M., Xue, Q., Zhang, M., et al. 2024, ApJL, 975, L22
Whittaker, E. A., Malik, M., Ih, J., et al. 2022, AJ, 164, 258
Xue, Q., Bean, J. L., Zhang, M., et al. 2024, ApJL, 973, L8
Xue, Q., Zhang, M., Coy, B. P., et al. 2025, ApJL, 995, L52
Zhang, M., Hu, R., Inglis, J., et al. 2024, ApJL, 961, L44
Zieba, S., Kreidberg, L., Coy, B. P., et al. 2026, NatAs, 10, 1129
Zieba, S., Kreidberg, L., Ducrot, E., et al. 2023, Natur, 620, 746